

Modeling and Simulation of A Laser Deposition Process

Frank Liou*, Zhiqiang Fan*, Heng Pan*, Kevin Slattery**, Mary Kinsella+, Joseph Newkirk*, and Hsin-Nan Chou**

*University of Missouri – Rolla, Rolla, MO, 65409

** The Boeing Company

+ AFRL/MLLMP

Reviewed, accepted September 4, 2007

Abstract

A laser deposition process involves the supply of metallic powders into a laser-heated spot where the powder is melted and forms a melt puddle which quickly solidifies into a bead. In order to design an effective system, the laser beam, the powder beam, and their interactions need to be fully understood. In this paper, the laser-material interaction within the melt pool is reported using a multi-scale model: a macroscopic model to model mass, heat, and momentum transfer. Experiments were also conducted to validate the simulation model.

Introduction

The direct laser deposition (DLD) process is an extension of the laser cladding process for rapid prototyping of fully dense metal components. It offers the ability to make a metal component directly from CAD drawings. It involves the supply of metallic powders into a laser-heated spot where the powder is melted and forms a melt puddle which quickly solidifies into a bead as shown in Figure 1. The thermal behavior of the melt pool in which powder is injected is critical for part quality. This paper uses simulation and experiments to investigate the effect of the process parameters: laser power, powder mass flow, and scanning speed on the melt pool thermal behavior. During the laser deposition process, several defects, such as porosity and cracks, should be paid attention to. Cracks initiate corrosion fracture and reduce fatigue strength of the deposited parts. Cracks are caused by the residual stresses created by the high thermal gradient built up during the cooling stage. Residual stresses can be reduced by a reduction of the cooling rate. This can be achieved by preheating the substrate. Moreover, the preheating causes a better absorption of the laser beam and further it is possible to melt more powder in the larger melting pool and enhance the bonding. Usually the preheating is performed in such a manner that a very small melting of the substrate material occurs without powder injection.

Thermal analysis of the laser deposition process is very important for optimization of the process. If the substrate surface temperatures remain too low, wetted deposit material is limited. In that case,

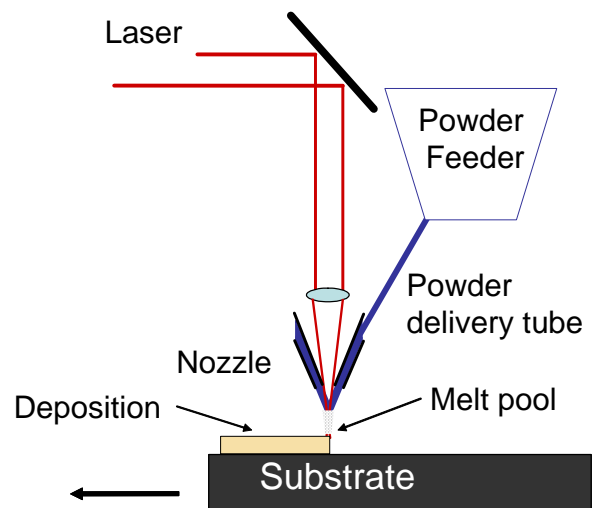


Fig 1 Laser-powder interaction at melt pool in a direct laser deposition (DLD) process.

irregularly shaped tracks with a lot of cracks, porosity and a poor bonding, are produced. However, if an extremely high temperature of the substrate surface is reached, severe melting of the substrate occurs. The high degree of dilution can deteriorate the clad properties. A comprehensive numerical model has been developed that allows the prediction of temperature distribution and melt pool dynamics. This model simulates the coaxial laser deposition process with powder injection, and considers most of the associated phenomena, such as melting, solidification, evaporation, evolution of the free surface, and powder injection. Input parameters for this model are laser machining parameters and properties of the laser beam, as well as material properties and laser beam absorption. To get more accurate predictions, a finer grid needs to be used. This, together with the iterative nature of the numerical algorithms, causes the model computationally not to be very efficient. In this paper an analytical model is applied to the preheating process (without powder injection) to increase the computational efficiency, while the actual deposition process with powder injection still uses the numerical model. The outputs, and the temperature distribution of the substrate, are used as the initial conditions of the numerical model.

In this study, a coaxial diode laser deposition system, LAMP (developed at UMR), is considered for simulations and experiments. The blown powder method is used to deliver powder. As the primary laser in the LAMP system, the diode laser is used. Material of both powder and substrates is Ti-6Al-4V, which is widely used in the aerospace industry.

Melt Pool Governing Equations

Figure 2 shows a schematic diagram of the calculation domain, including the substrate, melt pool, remelted zone, deposited layer and part of the gas region. In the laser deposition process, melting and solidification cause the phase transformation at the solid/liquid interface. A mushy zone containing solid and liquid is formed. In this study the continuum model [Bennon87a, Bennon87b] is adopted to derive the governing equations.

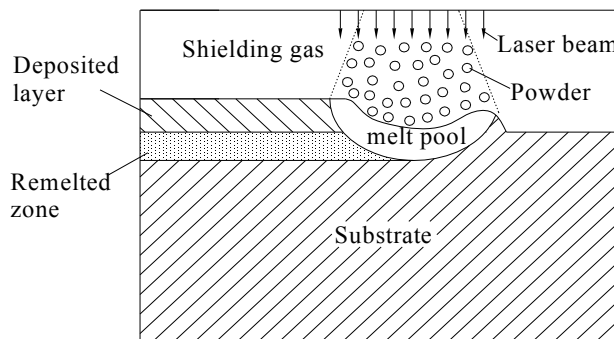


Fig. 2. Schematic of the calculation domain.

The assumptions for the system of governing equations include: (1) the fluid flow in the melt pool is a Newtonian, incompressible, laminar flow; (2) the solid and liquid phases in the mushy zone are in local thermal equilibrium; (3) the solid phase is rigid; and (4) isotropic permeability exists. For the system of interest, the conservation equations for mass, momentum and energy are summarized as follows:

Continuity

$$\frac{\partial \rho}{\partial t} + \nabla \cdot (\rho \vec{V}) = 0 \quad (1)$$

Momentum

$$\frac{\partial}{\partial t} (\rho \vec{V}) + \nabla \cdot (\rho \vec{V} \vec{V}) = \nabla \cdot \left(\mu_l \frac{\rho}{\rho_l} \nabla \vec{V} \right) - \nabla p - \frac{\mu_l}{K} \frac{\rho}{\rho_l} (\vec{V} - \vec{V}_s) + \rho \vec{g} + S \quad (2)$$

Energy

$$\frac{\partial(\rho h)}{\partial t} + \nabla \cdot (\rho \vec{V} h) = \nabla \cdot (k \nabla T) - \nabla \cdot (\rho (h_l - h) (\vec{V} - \vec{V}_s)) \quad (3)$$

In equations (1)-(3), the continuum density, specific heat, thermal conductivity, vector velocity, and enthalpy are defined as follows:

$$\begin{aligned} \rho &= g_s \rho_s + g_l \rho_l & c &= f_s c_s + f_l c_l & k &= g_s k_s + g_l k_l \\ \vec{V} &= f_s \vec{V}_s + f_l \vec{V}_l & h &= f_s h_s + f_l h_l \end{aligned} \quad (4)$$

The liquid fraction temperature relationship is given by:

$$g_l = \begin{cases} 0 & \text{if } T < T_s \\ \frac{T - T_s}{T_l - T_s} & \text{if } T_s \leq T \leq T_l \\ 1 & \text{if } T > T_l \end{cases} \quad (5)$$

The other volume and mass fractions can be obtained by:

$$f_l = \frac{g_l \rho_l}{\rho} \quad f_s = \frac{g_s \rho_s}{\rho} \quad g_s + g_l = 1 \quad f_s = 1 - f_l \quad (6)$$

The phase enthalpy for the solid and the liquid can be expressed as:

$$h_s = \int_0^T c_s(T) dT \quad h_l = \int_0^{T_s} c_s(T) dT + \int_{T_s}^T c_l(T) dT + L_m \quad (7)$$

where L_m is the latent heat of melting.

Permeability, K , is assumed to vary with liquid volume fraction according to the Carman - Kozeny equation [Carman37] derived from Darcy's law:

$$K = \frac{g_l^3}{C(1-g_l)^2} \quad (8)$$

where the parameter C is a constant depending on the morphology and size of the dendrites in the mushy zone. The S is a source term that is defined below.

Solid/liquid interface

The solid/liquid interface is implicitly tracked by the continuum model [Bennon87a, Bennon87a]. In the solid phase region and liquid phase region, the third term on the right-hand side of Eq. (2) vanishes. This is because in the solid phase region $\vec{V} = \vec{V}_s = 0$ and in liquid phase region $K \rightarrow \infty$ since $g_l = 1$. So this term is only valid in the mushy zone.

Free surface

The liquid/vapor interface, or the free surface of the melt pool, is very complex due to surface tension, thermocapillary force, and impaction of the powder injection. In this study, the Volume-Of-Fluid (VOF) method [Hirt81] is employed to track the evolution of the moving free surface of the melt pool. The melt pool configuration is defined in terms of a volume of fluid function, $F(x,y,t)$, which represents the volume of fluid per unit volume and satisfies the conservation equation:

$$\frac{\partial F}{\partial t} + (\mathbf{V} \cdot \nabla) F = 0 \quad (9)$$

Source term

The source term, S, in the momentum equation is contributed by the interface forces acting on the free surface, such as surface tension, etc. In this study, the continuum surface force (CSF) model [Brackbill92] is used to reformulate the surface force. In its standard form, surface tension is formulated as [Brackbill92]:

$$\vec{F}_s(\vec{x}_s) = \hat{n} \gamma \kappa + \nabla_s \gamma \quad (10)$$

where $\vec{F}_s(\vec{x}_s)$ is the net surface force at a point \vec{x}_s on a interface S. \hat{n} is a unit normal to S at the point \vec{x}_s , which is given by:

$$\hat{n} = \frac{\vec{n}}{|\vec{n}|} \quad (11)$$

where \vec{n} is the surface normal vector and can be computed from the gradient of the VOF function:

$$\vec{n} = \nabla F \quad (12)$$

∇_s is the gradient along a direction tangential to the interface, which is defined as:

$$\nabla_s = \nabla - \nabla_N = \nabla - \hat{n}(\hat{n} \cdot \nabla) \quad (13)$$

γ and κ represent surface tension coefficient and curvature, respectively. κ is given in [Prakash89]:

$$\kappa = -(\nabla \cdot \hat{n}) = \frac{1}{|\bar{n}|} \left[\left(\frac{\bar{n}}{|\bar{n}|} \cdot \nabla \right) |\bar{n}| - (\nabla \cdot \bar{n}) \right] \quad (14)$$

By using the CSF model, the surface force \vec{F}_s is reformulated into a volume force \vec{F}_b as follows:

$$\vec{F}_b = \vec{F}_s |\bar{n}| \frac{F}{\langle F \rangle} = \vec{F}_s |\nabla F| \frac{F}{\langle F \rangle} \quad (15)$$

where $\langle F \rangle$ is the averaged F value across the free surface. Thus, the source term S in equation (2) is formulated as:

$$S = (\bar{n} \gamma \kappa + \nabla_s \gamma) |\nabla F| \frac{F}{\langle F \rangle} \quad (16)$$

Boundary Conditions

The boundary conditions at the free surface satisfy the following equation:

$$k \frac{\partial T}{\partial n} = \frac{\eta(P_{laser} - P_{atten})}{\pi R^2} - h_c(T - T_\infty) - \varepsilon \sigma(T^4 - T_\infty^4) - \dot{m}_e L_v \quad (17)$$

where terms on the right-hand side are laser irradiation, convective heat loss, radiation heat loss and evaporation heat loss, respectively. P_{laser} is the power of laser beam, P_{atten} the power attenuated by the powder cloud, R is the laser beam radius, η the laser absorption coefficient. P_{atten} is calculated according to Frenk's et al. model [Frenk97] with a minor modification:

$$P_{atten} = P_{laser} \left[1 - \exp \left(- \frac{3Q_{ext} \dot{m} l}{\pi \rho r_p D_{jet} v_p} \right) \right] \quad (18)$$

where \dot{m} denotes the powder mass flow rate, l is the stand-off distance from the nozzle exit to the substrate, ρ is powder density, r_p is the radius of the powder particle, D_{jet} is the diameter of the powder jet, v_p is the powder injection velocity, and Q_{ext} is the extinction coefficient. It is assumed that the extinction cross section is close to the actual geometrical cross section, and Q_{ext} takes a value of unity. In the evaporation term, \dot{m}_e is the evaporation mass flux and L_v is the

latent heat of evaporation. According to Choi et al.'s overall evaporation model [Choi87], \dot{m}_e is of the form:

$$\log \dot{m}_e = A + 6.1210 - \frac{18836}{T} - 0.5 \log T \quad (19)$$

where A is a constant dependent on the material.

The boundary conditions at the bottom, left and right wall satisfy the following equations:

$$k \frac{\partial T}{\partial n} = -h_c(T - T_\infty) \quad (20)$$

$$u = 0 \quad v = 0 \quad (21)$$

Powder injection

Powder particles that inject onto the top surface can be classified into three categories. 1) Those powder particles that have not been melted during their passage and hit the solid part of the substrate will deflect and lose; 2) Those powder particles that have been melted before they arrive on the substrate and impact the solid part of the substrate will stick to the surface of the substrate; and 3) Those powder particles that fall into the melt pool including melted and unmelted will merge and mix with the molten liquid in the melt pool [Han04]. In this study, the powder particles belonging to the last two cases were modeled.

Numerical simulation

Simulation is performed based on the capability of the experimental facilities to compare the simulation results with the experimental measurements. A continuous wave diode laser with an 808 nm wavelength is considered as the energy source. The laser intensity distribution is uniform. For substrates, Ti-6Al-V4 plates with a thickness of 0.25 inch are selected. Ti-6Al-V4 powder particles with a diameter from 40 to 140 μm are used as deposit material. The laser absorption coefficient is measured by Sparks et al. [Sparks06]. The material properties and the main process parameters are shown in Table 1. Figure 3 shows typical simulation results for normal deposition and lack of fusion.

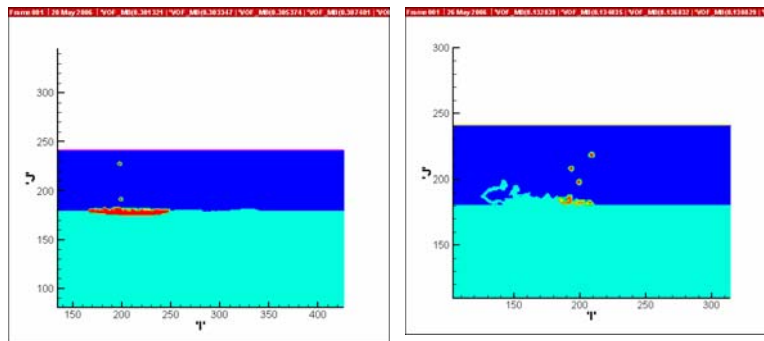


Fig. 3. Typical results for simulation of normal deposition (left) and lack of fusion (right).

Experimental Study

The experiments were performed on the LAMP system which consists of a diode laser, powder delivery unit, 5-axis CNC machine, and monitoring subsystem. The laser system used in the study was Nuvonyx (Nuvonyx Inc.) ISL-1000M Laser Diode System which combines state-of-the-art micro-optics with laser diodes to produce the only single wavelength fiber coupled direct diode laser at power levels up to 1000 watts CW. The laser emits at 808 nm and operates in the continuous wave (CW) mode. The substrates have dimensions of 2.5×2.5×0.4 in. The Ti-6Al-4V samples were irradiated using a laser beam with a beam spot diameter of 2.5 mm.

Table 1. Material properties for Ti-6Al-4V and main process parameters

Nonmenclature	Symbol	Value (unit)
Melting temperature	T_m	1900.0K
Liquidus temperature	T_l	1923.0K
Solidus temperature	T_s	1877.0K
Evaporation temperature	T_v	3533.0K
Solid specific heat at constant pressure [Kelly04]	c_{ps}	$\begin{cases} 483.04 + 0.215T & T \leq 1268K \\ 412.7 + 0.1801T & 1268 < T \leq 1923 \end{cases} \quad J/kg \ K$
Liquid specific heat at constant pressure [Mills02]	c_{pl}	831.0 J/kg K
Thermal conductivity [Kelly04]	k	$\begin{cases} 1.2595 + 0.0157T & T \leq 1268K \\ 3.5127 + 0.0127T & 1268 < T \leq 1923 \\ -12.752 + 0.024T & T > 1923 \end{cases} \quad W/m \ K$
Solid density [Mills0]	ρ_s	$4420 - 0.154 (T - 298 \text{ K})$
Liquid density [Mills0]	ρ_l	$3920 - 0.68 (T - 1923 \text{ K})$
Latent heat of fusion [Mills0]	L_m	$2.86 \times 10^5 \text{ J/kg}$
Latent heat of evaporation	L_v	$9.83 \times 10^6 \text{ J/kg}$
Dynamic viscosity	μ	$3.25 \times 10^{-3} \text{ N/m s (1923K)} \quad 3.03 \times 10^{-3} \text{ (1973K)}$ $2.66 \times 10^{-3} \text{ (2073K)} \quad 2.36 \times 10^{-3} \text{ (2173K)}$
Radiation emissivity [Lips 05]	ϵ	$0.1536 + 1.8377 \times 10^{-4} (T - 300.0 \text{ K})$
Laser absorption coefficient [Sparks04]	η	0.4
Powder particle diameter	D_p	40-140 μm
Shielding gas pressure	P_g	5 psi
Ambient temperature	T_∞	300K
Convective coefficient	h_c	10 $\text{W/m}^2 \text{ K}$

In order to validate the model predictions, single path deposition experiments are conducted. The comparisons between model predictions and experimental results are conducted in terms of melt pool peak temperature. The melt pool peak temperature is calibrated through the dual-wavelength non-contact temperature sensor, which can effectively decrease the disturbance from the powder and other dusts.

Comparisons and discussions

Fig. 4 and Fig. 5 show the comparisons between experimental measurements and model predictions. Fig. 4 shows the effects of laser power on melt pool peak temperature. It can be seen that an increase in the laser power will increase the melt pool temperature. This is easy to

understand. As the laser power increases, more power is available for melting the substrate. Fig. 5 shows the effects of laser scanning speed on the melt pool peak temperature. An increase in the laser scanning speed will decrease the melt pool peak temperature. This is because, as scanning speed decreases, the laser material interaction time is extended.

From Figs. 4-5, one can see that the general trend between experimental measurements and model predictions is consistent. At a different power intensity level, there is a different error from 10 K (about 0.5%) to 121K (about 5%). It can be seen that at a higher power intensity level, there is a bigger error between measurements and predictions. This is because the numerical model is two-dimensional. It does not consider the heat and mass transfer in the third direction. At a higher power intensity level, heat and mass transfer in the third dimension are more significant.

The errors between experimental measurements and model predictions are analyzed to mainly come from the following aspects: (1) The two-dimensional nature of the numerical model; (2) The thermo-physical properties taken for the analytical model; (3) The uncertainties of the material properties and the appropriateness of the sub-models for the numerical model; (4) Boundary conditions. Adiabatic boundary conditions are assumed in the analytical model and the numerical model for the bottom surface and side surfaces. Measurements also have been taken to achieve such boundary conditions in experiments. But it is hard to get absolute adiabatic boundary conditions.

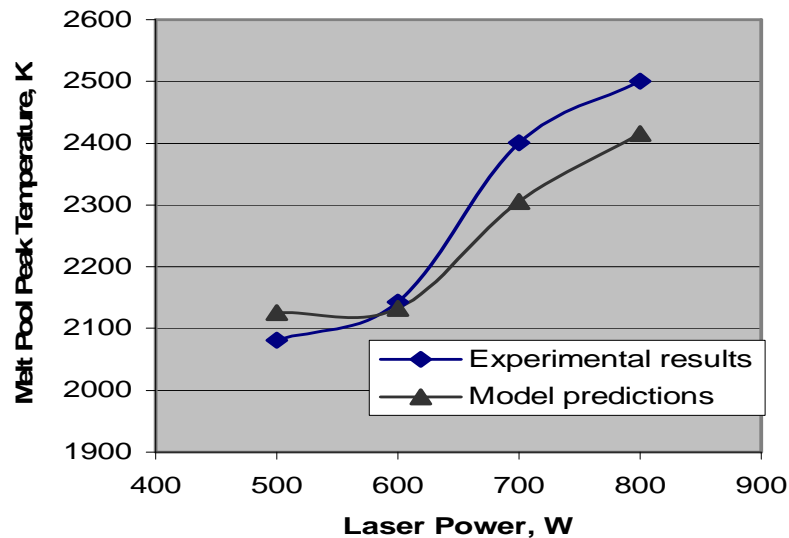


Fig. 4 Comparisons between experimental measurements and model predictions at a constant powder mass flow rate of 5g/min and a constant laser scanning speed of 20 inch/min. (For actual deposition)

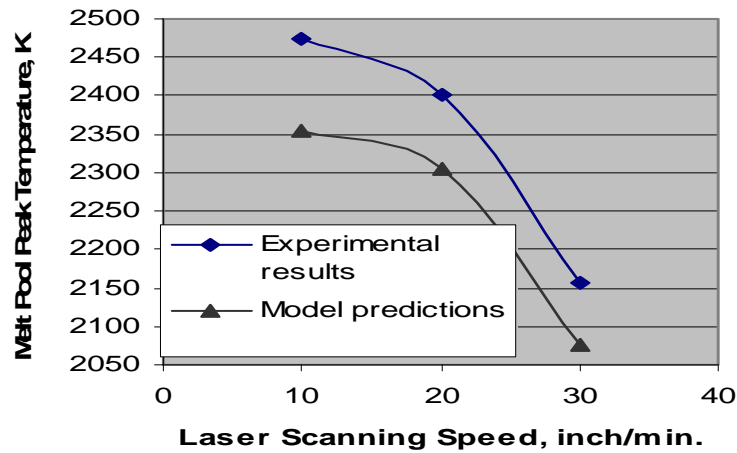


Fig. 5 Comparisons between experimental measurements and model predictions at a constant powder mass flow rate of 5g/min and a constant laser power of 700 W. (For actual deposition)

The simulation model was also used to predict the lack of fusion to deposit Ti64. Twenty-eight Ti64 samples were built to validate the simulation model. The idea was to use the simulation model to predict the lack of fusion, and the corresponding laser power is used as nominal power. The depositions are then based on Nominal, Nominal +/- 10%, Nominal +/- 20%, and Nominal +/- 30%. The nominal is about 600 W for the direct diode laser. The nominal power is then set at 600W with a travel speed (scanning speed) at 10ipm and powder flow rate ~ 5g/min. The experiment was performed at -30% (420W), -20% (480W), -10% (540W), nominal (600W), 10%(660W), 20%(720W), 30% (780W). If the predicted model for lack of fusion is accurate, about 50% of the parts will be observed as lack of fusion. Seven samples of thick walls are shown in Figure 6. It can be observed that most samples with lower power than the nominal showed obvious porosities on the sample surface.



(a) Sample produced at -30% laser power



(b) Sample produced at -20% laser power



(c) Sample produced at -10% laser power



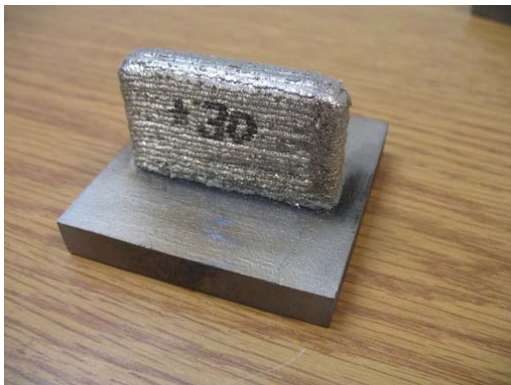
(d) Sample produced at nominal laser power



(e) Sample produced at +10% laser power



(f) Sample produced at +20% laser power



(g) Sample produced at +30% laser power

Fig 6. A thick wall Ti64 part produced at various laser powers (Nominal, Nominal +- 10%, Nominal +- 20%, and Nominal +- 30%) in the UMR LAMP lab. Lack of fusion can be observed from some surfaces of the samples with lower power.

Conclusions

The thermal behavior of melt pool is the most critical phenomenon in laser deposition. An analytical model for thermal analysis of temperature rise due to a moving heat source is combined into a comprehensive heat transfer and fluid flow numerical model for the laser deposition process. The analytical model is used for the preheating process before the actual

laser deposition with powder injection. And the numerical model is used for the actual laser deposition process. Thus the outputs of the analytical model are used as the inputs of the numerical model. Experiments have been conducted to validate the model predictions. A consistent general trend is found between experimental measurements and the model predictions. The sources of the errors have also been analyzed.

Acknowledgements

This research was supported by the National Science Foundation Grant Number DMI-9871185, the grant from the U.S. Air Force Research Laboratory contract # FA8650-04-C-5704, and UMR Intelligent Systems Center. Their support is greatly appreciated.

References

- Bennon, W.D., F.P. Incropera, A continuum model for momentum, heat and species transport in binary solid-liquid phase change systems-I. Model formulation, *International Journal of Heat and Mass Transfer* 30 (1987a) 2161-2170.
- Bennon, W.D., F.P. Incropera, A continuum model for momentum, heat and species transport in binary solid-liquid phase-change systems--II. Application to solidification in a rectangular cavity, *International Journal of Heat and Mass Transfer* 30 (1987b) 2171-2187.
- Brackbill, J. U., D. B. Kothe, C. Zemach, A continuum method for modeling surface tension, *Journal of Computational Physics* 100 (1992) 335-354.
- Carman, P.C., Fluid flow through granular beds, *Trans. Institution Chem. Engrs.* 15 (1937) 150-166.
- Choi, M., R. Greif, M. Salcudean, A study of the heat transfer during arc welding with applications to pure metals or alloys and low or high boiling temperature materials, *Numerical Heat Transfer* 11 (1987) 477-491.
- Frenk, A., M. Vandyoussefi, J. Wagniere, A. Zryd, W. Kurz, Analysis of the laser-cladding process for stellite on steel, *Metallurgical and Materials Transactions B (USA)* 28B (1997) 501-508.
- Han, L., F.W. Liou, K.M. Phatk, Modeling of laser cladding with powder injection, *Metallurgical and Materials Transactions B* 35B (2004) 1139-1150.
- Hirt, C.W., B.D. Nichols, Volume of fluid (VOF) method for the dynamics of free boundaries, *Journal of Computational Physics* 39 (1981) 201-225.

- Kelly, S.M., Thermal and microstructure modeling of metal deposition processes with application to Ti-6Al-4V, Ph.D. thesis, Virginia Polytechnic Institute and State University, 2004.
- Mills, K. C., Recommended values of thermophysical properties for selected commercial alloys, Woodhead, Cambridge, 2002.
- Lips, Tobias, Bent Fritsche, A comparison of commonly used re-entry analysis tools, *Acta Astronautica* 57 (2005) 312-323.
- Prakash, C., V. Voller, On the numerical solution of continuum mixture model equations describing binary solid-liquid phase change, *Numerical Heat Transfer* 15B (1989) 171-89.
- Sparks, Todd E., Zhiqiang Fan, Measurement of laser absorption coefficient of several alloys for diode laser, unpublished report, 2006.